Modeling flow and scalar dispersion around Cheomseongdae

Jae-Jin Kim[†]

Climate Environment System Research Center, Seoul National University, Seoul 151-742, Korea

Hyo-Jong Song[‡] and Jong-Jin Baik[‡†]

School of Earth and Environmental Sciences, Seoul National University, Seoul 151-742, Korea

Abstract. Flow and scalar dispersion around Cheomseongdae are numerically investigated using a three-dimensional computational fluid dynamics (CFD) model with the renormalization group (RNG) $k - \varepsilon$ turbulence closure scheme. Cheomseongdae is an ancient astronomical observatory in Gyeongju, Korea, and is chosen as a model obstacle because of its unique shape, that is, a cylinder-shaped architectural structure with its radius varying with height. An interesting feature found is a mid-height saddle point behind Cheomseongdae. Different obstacle shapes and corresponding flow convergences help to explain the presence of the saddle point. The predicted size of recirculation zone formed behind Cheomseongdae increases with increasing ambient wind speed and decreases with increasing ambient turbulence intensity. The relative roles of inertial and eddy forces in producing cavity flow zones around an obstacle are conceptually presented. An increase in inertial force promotes flow separation. Consequently, cavity flow zones around the obstacle expand and flow reattachment occurs farther downwind. An increase in eddy force weakens flow separation by mixing momentum there. This results in the contraction of cavity flow zones and flow reattachment occurs less far downwind. An increase in ambient wind speed lowers predicted scalar concentration. An increase in ambient turbulence intensity lowers predicted maximum scalar concentration and acts to distribute scalars evenly.

Keywords: computational fluid dynamics; renormalization group $k - \varepsilon$ turbulence model; Cheomseongdae; recirculation zone; saddle point; flow reattachment; scalar dispersion.

1. Introduction

Advances in computing power have accelerated the use of computational fluid dynamics (CFD) models in investigating environmental and geophysical fluid flows. Large-eddy simulation (LES) models receive much attention because the physical assumptions are known to be better than those in Reynolds-averaged Navier-Stokes equations (RANS) models and intermittence as well as

---

† Postdoctoral Fellow, Present Affiliation: Korea Meteorological Administration
‡ Graduate Student
‡† Associate Professor, Corresponding Author, E-mail: jjbaik@snu.ac.kr

transience can be well simulated in turbulent flow modeling. However, expensive computing times restrict their use in environmental and geophysical applications. RANS models demand less expensive computing times, but they need to parameterize turbulence properly. One of the turbulence closure schemes most widely used in RANS models is a standard two-equation ($k - \varepsilon$) turbulence closure scheme. However, this scheme is known to overestimate turbulent kinetic energy in simulating flow separations around obstacles (Castro and Apsley 1997). To overcome this defect, a renormalization group (RNG) $k - \varepsilon$ turbulence closure scheme has been developed (Yakhot and Orszag 1986, Yakhot, *et al.* 1992). Recently, CFD models employing the RNG $k - \varepsilon$ turbulence closure scheme have been successfully applied to building-scale flow and pollutant dispersion simulations (e.g. Tutar and Oguz 2002, Brown and Dabberdt 2003, Kim and Baik 2004).

Understanding building-scale flow and dispersion is a basis for understanding urban-scale flow and dispersion and can help to solve numerous urban environmental problems such as ensuring sunshine, reducing heat island effects, optimizing ventilation, etc. (Chan, *et al.* 2001). Extensive studies have been made to understand mean flow, turbulence statistics, and scalar dispersion around obstacles. These include numerical (e.g. Lübcke, *et al.* 2001, Smith, *et al.* 2001, Sada and Sato 2002, Jiang, *et al.* 2003), fluid experimental (e.g. Hussein and Martinuzzi 1996, Nigim 1996, Meroney, *et al.* 1999), and observational (e.g. Jones and Griffiths 1984, Higson, *et al.* 1994) studies. In almost all previous numerical and fluid experimental studies, obstacles considered are simply shaped (e.g. cubical or rectangular) and in terms of obstacle aspect ratio relatively short. Buildings in urban areas have various shapes and heights. Especially, buildings in central business districts are tall and slender. Therefore, it might be interesting to simulate and understand flow and dispersion around an obstacle that is complex compared with the simple obstacles in geometry. This will enhance our understanding of flow and dispersion in the presence of complex obstacles. This motivated the present study.

This study aims to find a three-dimensional flow structure around a single but rather complex obstacle and investigate the effects of ambient wind speed and turbulence intensity on mean flow and scalar dispersion around the obstacle. For this, Cheomseongdae, an ancient astronomical observatory in Gyeongju, Korea, is selected as a model obstacle because of its unique shape and also its historical and scientific importance. Cheomseongdae is a cylinder-shaped architectural structure with its radius varying with height. Thus, this study will provide additional insights into flow and scalar dispersion around obstacles. In section 2, an architectural description of Cheomseongdae is given. In section 3, the numerical model used is briefly described and experimental design is given. In section 4, model simulation results are presented and discussed. A summary is given in section 5.

2. Cheomseongdae

Cheomseongdae (Fig. 1) was built for astronomical observation by Queen Seondeok of the Silla dynasty in the mid-seventh century. It consists of a stereobate at the bottom, a pillar, and a pavilion part at the top. It is presumed that astronomers would observe stars and astronomical phenomena, sitting on the pavilion part. The horizontal cross-section of the stereobate is square and that of the pillar is circular, reflecting an ancient outlook, at that time, on the world that the earth is square and the sky is round. The stereobate consists of 29 stones. This number corresponds to the days in one month in the lunar calendar. The pillar is made up of 27 stairs, symbolizing that Queen Seondeok is the 27th ruler of the Silla dynasty. It has a window-like hole at the middle height. There are 12

Fig. 1 Cheomseongdae

stairs above and below the hole, standing for 12 months. 366 stones constituting the pillar and pavilion part mean the number of days in one year. The height of Cheomseongdae is 9.16 m, with the thicknesses of the stereobate, pillar, and pavilion part being 0.36 m, 8.19 m, and 0.61 m, respectively. The side length of the square stereobate is 5.18 m long. The radius of the pillar decreases with height from 2.55 m to 1.46 m. The side length of the pavilion part is 3.06 m long. The aspect ratio (ratio of the height to the width) of Cheomseongdae ranges from 1.77 to 3.14, indicating that Cheomseongdae is a relatively tall obstacle.

3. Numerical model and experimental design

The numerical model used in this study is the same as that of Kim and Baik (2004). The performance of the numerical model is evaluated against the wind tunnel data of Brown, *et al.* (2000) in that paper. The model considers a three-dimensional, nonhydrostatic, nonrotating, incompressible flow system. The governing equation set includes the momentum equations, the mass continuity equation, and the transport equation for passive scalar. For turbulence parameterization, the two-equation (turbulent kinetic energy k and its dissipation rate ε) turbulence closure scheme based on the RNG theory is implemented. The governing equations are numerically solved using the finite volume method. For further details of the numerical model, see Kim and Baik (2004).

To increase computational efficiency, a non-uniform grid system with 116, 89, and 83 cells in the x-, y-, and z-directions, respectively, is used (Fig. 2). The dimension of the smallest cell is 0.2 m × 0.2 m × 0.2 m. The expansion ratio in the present non-uniform grid system does not exceed 1.1. The dimension of the largest cell is 2.1 m × 2.1 m × 1.5 m. The domain size is 133.0 m × 75.5 m × 72.6 m in the x-, y-, and z-directions, respectively. The time step used is 0.1 s. A larger time step can be
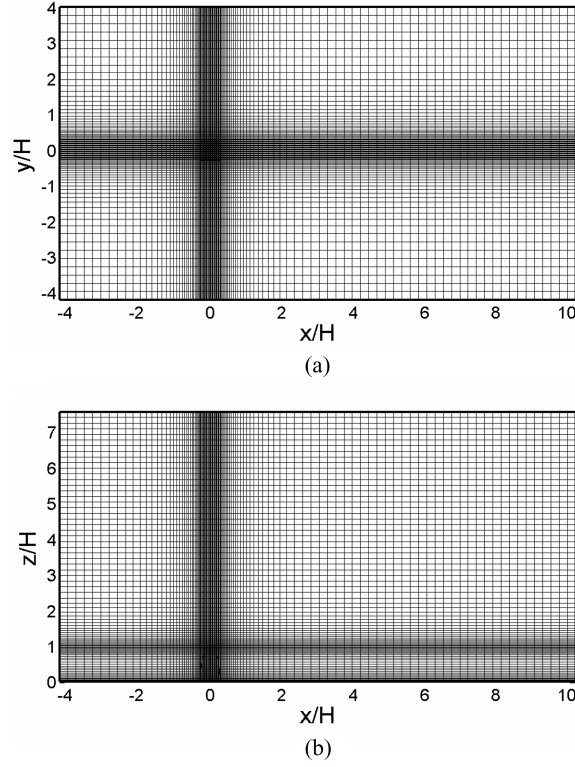
Fig. 2 (a) Horizontal and (b) vertical view of the computational domain and grid system. The horizontal and vertical coordinates are normalized by the height of Cheomseongdae (H)

used for stable simulations because the time differencing scheme is implicit. The numerical model is integrated up to $t = 30$ min. The ambient wind blows from left to right (see Fig. 2). At the inflow boundary, the vertical profiles of ambient horizontal wind speed (x-direction), turbulent kinetic energy, and its dissipation rate are specified as

$$U(z) = U_r \left(\frac{z}{z_r} \right)^{0.299} \tag{1}$$

$$k(z) = a \frac{U^2(z)}{2} \tag{2}$$

$$\varepsilon(z) = \frac{C_\mu^{3/4} k^{3/2}}{\kappa z} \tag{3}$$

Here, z_r is the reference height ($= 10$ m), U_r is the reference horizontal wind speed at $z = z_r$, C_μ is a constant ($= 0.0845$), and κ is the von Karman constant ($= 0.4$). The constant a in Eq. (2) is a parameter that determines the ratio of turbulent kinetic energy to mean flow kinetic energy at the inflow boundary. At the lateral, upper, and outflow boundaries, a zero-gradient boundary condition is applied. At the solid surface, a wall boundary condition is applied.

Nine numerical experiments are performed with different meteorological conditions and obstacle

shapes. In the control experiment, U_r is 5 m s^{-1} and a is 0.005 (that is, turbulent kinetic energy is 0.5% of mean flow kinetic energy at the inflow boundary). Passive scalars are continuously released with an emission rate of 100 ppb s^{-1} from a point source located at $(x/H, y/H, z/H) = (-1.34, 0, 0.49)$ starting from $t = 10$ min. Notice that the origin of the coordinate system is the bottom center of Cheomseongdae. All simulation results presented below are at $t = 30$ min.

The mesh independence is understood to be geometry-dependent. In the present simulations, a non-uniform grid system with fine resolution near the solid surface is employed to resolve flow features well with computational efficiency. A better way would be to perform a simulation using a uniform grid system with a grid size of 0.2 m (finest grid size in the present simulations). Comparison of simulation results using the non-uniform and uniform grid systems would naturally enable us to test adequacy of the mesh refinement. Although adequacy of the mesh refinement is not tested in this study, results from the two simulations might be similar because the dimensions of simulated main flow features around Cheomseongdae (shown in section 4.1) are much larger than the smallest grid dimension. However, adequacy of the mesh refinement needs to be tested for this type of obstacle with an enhanced computing facility.

4. Results and discussion

4.1. Control experiment

We first examine the mean flow field in the control experiment. Based on the analysis of the simulated mean flow field, its three-dimensional structure around Cheomseongdae is schematically drawn in Fig. 3. In this study, the horizontal surface of the roof of Cheomseongdae is assumed to be a flat solid surface for simplicity. Flow impingement on the upwind face produces a stagnation point, resulting in upward motion above the stagnation point and downward motion below it. A horseshoe vortex is generated under the stagnation point. The horseshoe vortex expands downwind,
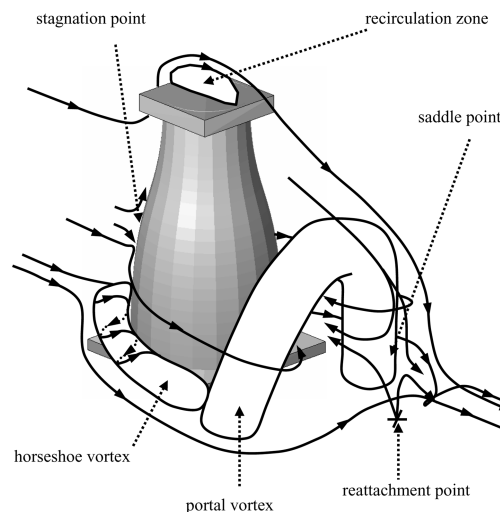

Fig. 3 Schematic of the simulated mean flow field around Cheomseongdae. The portal vortex drawn here is reduced in its size for the clarity of figure

wrapping around the lower part of Cheomseongdae. Flow separation near the upwind edge of the roof produces flow reattachment on the roof and a recirculation zone above it. Behind Cheomseongdae, a portal vortex whose ends touch down on the ground surface is generated. The vertical cross-section of the portal vortex at $y = 0$ is named as a recirculation zone. The horizontal cross-section of the portal vortex shows a double-vortex (or double-eddy) circulation behind Cheomseongdae (see Fig. 4(a)). The features mentioned above are commonly observed around obstacles (Hussein and Martinuzzi 1996, Becker, *et al.* 2002, Kim and Baik 2004).
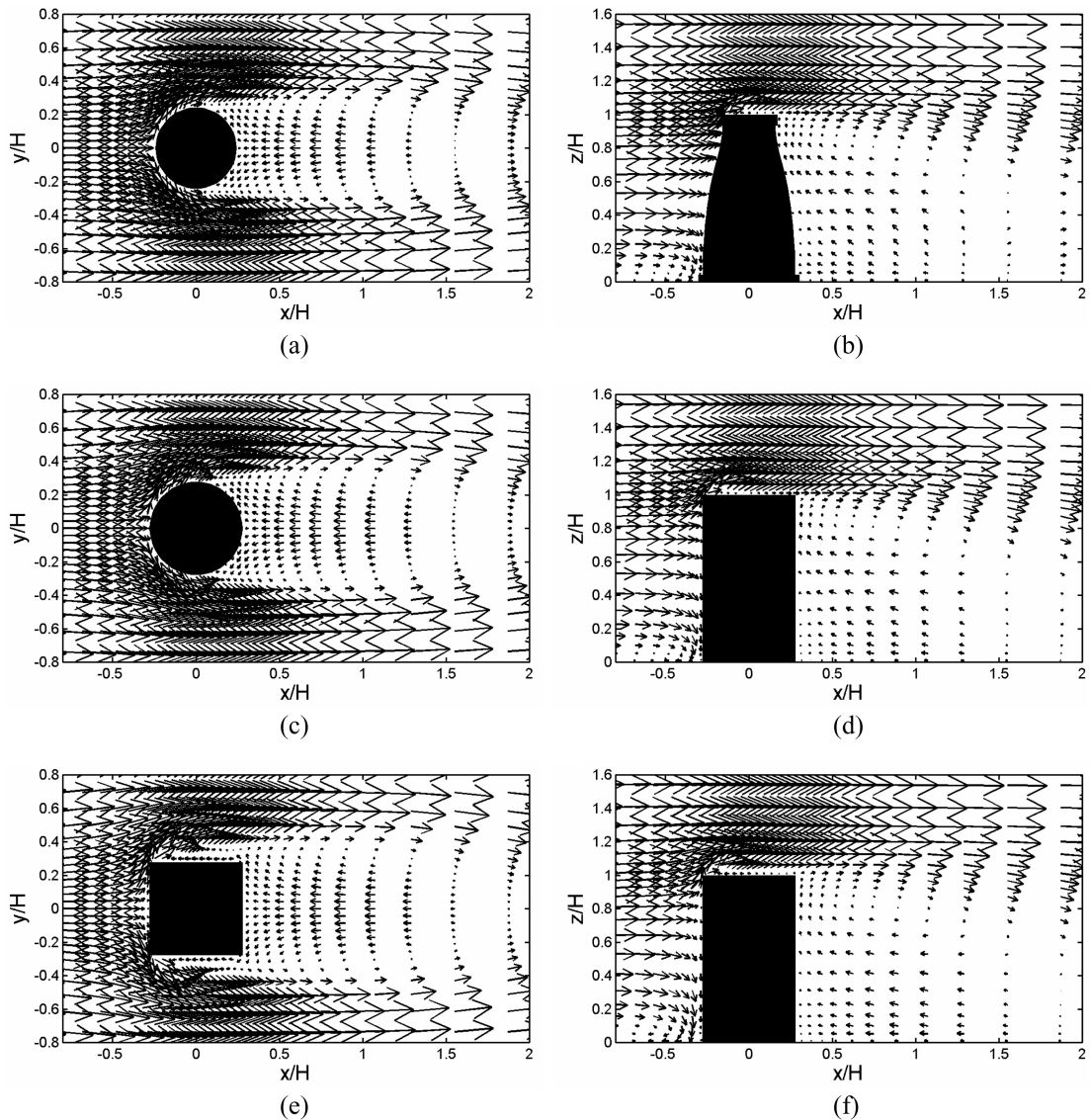

Fig. 4 Wind vector fields at $z/H = 0.49$ (left) and $y/H = 0$ (right) in the control experiment [(a) and (b)], cylinder [(c) and (d)], and square column [(e) and (f)] cases. The maximum wind vector lengths in (a), (b), (c), (d), (e), and (f) are 4.41, 7.44, 4.46, 7.45, 4.49, and 7.45 m s^{-1}, respectively

Behind the portal vortex, an interesting feature related to flow reattachment is simulated. Flow passing over Cheomseongdae does not reach the ground surface before meeting with flow from the lower layer. Typically, flow reattachment occurs on the ground surface behind a portal vortex and from there flow recovery starts. That is, flows passing over and going around an obstacle converge at some distance downwind on the ground surface for flow recovery. However, in the control experiment, flow going around Cheomseongdae goes upward and meets with flow passing over it, forming a saddle point at the middle height instead of achieving flow reattachment on the ground surface (Fig. 4(b)). The (horizontal) distance to the saddle point from the center of Cheomseongdae is $1.50H$. Then, flow starts to recover downwind. In spite of the presence of the saddle point, the location of flow reattachment on the ground surface can be considered as a location where flow reverses in its direction on the ground surface. Then, the distance to the flow reattachment from the center of Cheomseongdae is $1.70H$.

To find out whether the peculiar shape of Cheomseongdae is responsible for the presence of the saddle point at the middle height, numerical experiments are performed with two different obstacle shapes, a cylinder and a square column (designated as experiments A1 and A2, respectively). The diameter of the cylinder is set equal to the largest diameter of the pillar. The side length of the square column is set equal to that of the stereobate. The height of the cylinder/square column is the same as that of Cheomseongdae. A similar feature is simulated in experiment A1 (Fig. 4(d)). In experiment A2, flow recovery starts just at the reattachment point on the ground surface (Fig. 4(f)). A separation (or cavity) boundary is formed by flow impingement on the upwind face of the obstacle. The separated recirculation zones beside the square column are larger in experiment A2 (Fig. 4(e)) than in the control experiment (Fig. 4(a)) and in experiment A1 (Fig. 4(c)). Therefore, it takes a relatively longer time for flow to go around the square column. This explains why flow reattachment in experiment A2 occurs on the ground surface. It is thus noticed that the convergence of flow passing by a relatively tall obstacle occurs more quickly than that of flow passing over it.

We next examine the spatial distribution of passive scalars released from an upwind point source for 20 minutes. Fig. 5 shows the iso-surfaces of scalar concentrations. The scalar concentration is very high near the point source but very low elsewhere. The maximum concentration is 119 ppb, which is found at the point source location. In the cavity region behind Cheomseongdae, the scalar concentration is lower than 1% of its maximum. That is, only a small portion of scalars released is trapped in the cavity region. A scalar plume with a relatively high concentration is distributed around Cheomseongdae except for on its leeside (Fig. 5(b)). A scalar plume with a very low concentration covers Cheomseongdae and the cavity region (Figs. 5(c) and 5(d)). From Figs. 5(b) and 5(c), we can deduce how scalars are distributed in the cavity region of Cheomseongdae. Scalars near both sides of the cavity region at the middle height (Fig. 5(b)) enter into the inner cavity region. A budget analysis showed that the scalars enter from the outer region into the inner region mainly through a turbulent diffusion process. Then, the entered scalars are transported to the upwind region by reverse flow and to the upper layer by upward motion on the leeside. This explains why in the upper layer the scalar concentration is higher near the leeward face of Cheomseongdae than downwind (Fig. 5(c)). Near the ground surface, the scalar concentration in the cavity region is very low.

4.2. Effects of ambient wind speed and turbulence intensity

To investigate the effects of ambient wind speed and turbulence intensity on flow and scalar
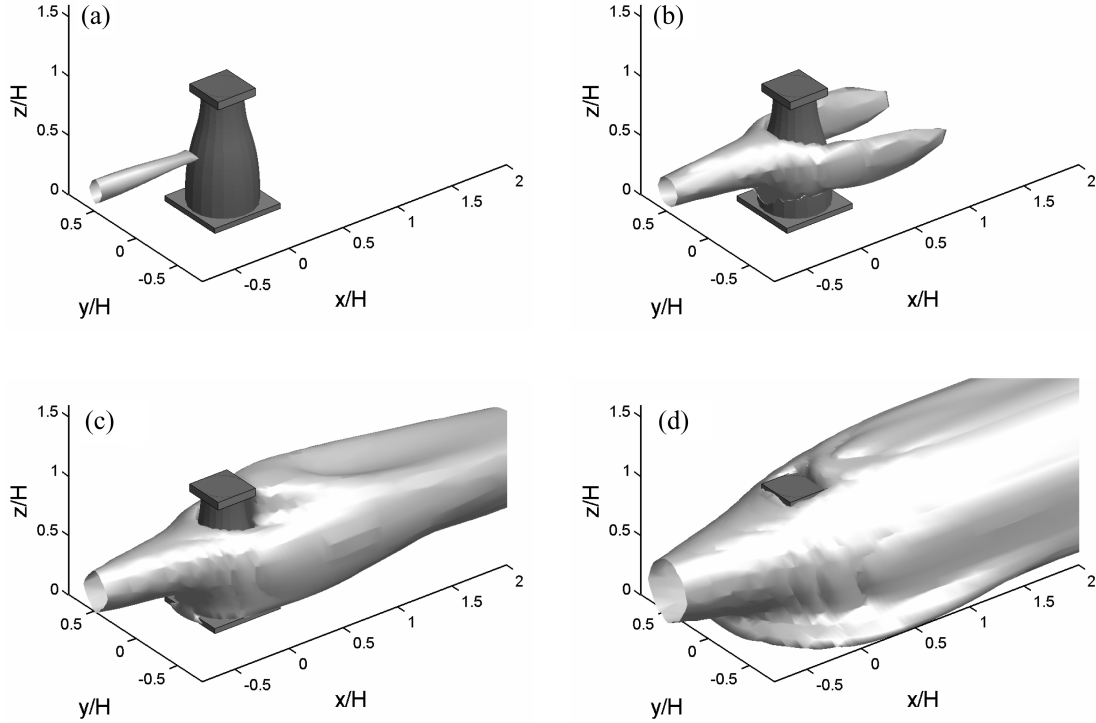
Fig. 5 Iso-surfaces of scalar concentrations of (a) 7.80 ppb, (b) 1.68 ppb, (c) 0.60 ppb, and (d) 0.12 ppb

dispersion around Cheomseongdae, six numerical experiments are performed with different inflow boundary conditions. In experiments performed to examine the effects of ambient wind speed, a is fixed as 0.005 [see Eq. (2)] and the horizontal wind speed at the reference height U_r [see Eq. (1)] varies: 1 m s^{-1} (experiment S1), 3 m s^{-1} (experiment S2), and 7 m s^{-1} (experiment S3) at the inflow boundary. Notice that in the control experiment a is 0.005 and U_r is 5 m s^{-1}. In experiments to examine the effects of ambient turbulence intensity, U_r is fixed as 5 m s^{-1} and a varies: 0.02 (experiment S4), 0.05 (experiment S5), and 0.10 (experiment S6) at the inflow boundary.

Fig. 6 shows simulated wind vector fields at $y/H = 0$ in experiments S1, S2, and S3. In experiment S1, a recirculation zone above the roof is not formed. As U_r increases further, a recirculation zone above the roof is formed and the recirculation strengthens (Figs. 6(b), 4(b), and 6(c)). The distance to the saddle point (also the flow reattachment point on the ground surface) increases with increasing U_r (Fig. 7(a)). The distance to the saddle point is $0.45H$, $1.20H$, and $1.60H$ and the distance to the flow reattachment point on the ground surface is $1.20H$, $1.55H$, and $1.70H$ in experiments S1, S2, and S3, respectively. This indicates that an increase in ambient wind speed results in an increase in the size of the recirculation zone behind Cheomseongdae.

The recirculation zone above the roof becomes weak as a increases (Figs. 4(b) and 8(a)) and eventually disappears in the cases of $a = 0.05$ and 0.10 (Figs. 8(b) and 8(c)). The distance to the saddle point (also the flow reattachment point) decreases with increasing a (Fig. 7(a)). The distance to the saddle point is $1.30H$, $1.05H$, and $0.85H$ and the distance to the flow reattachment point on the ground surface is $1.60H$, $1.50H$, and $1.30H$ in experiments S4, S5, and S6, respectively. Unlike
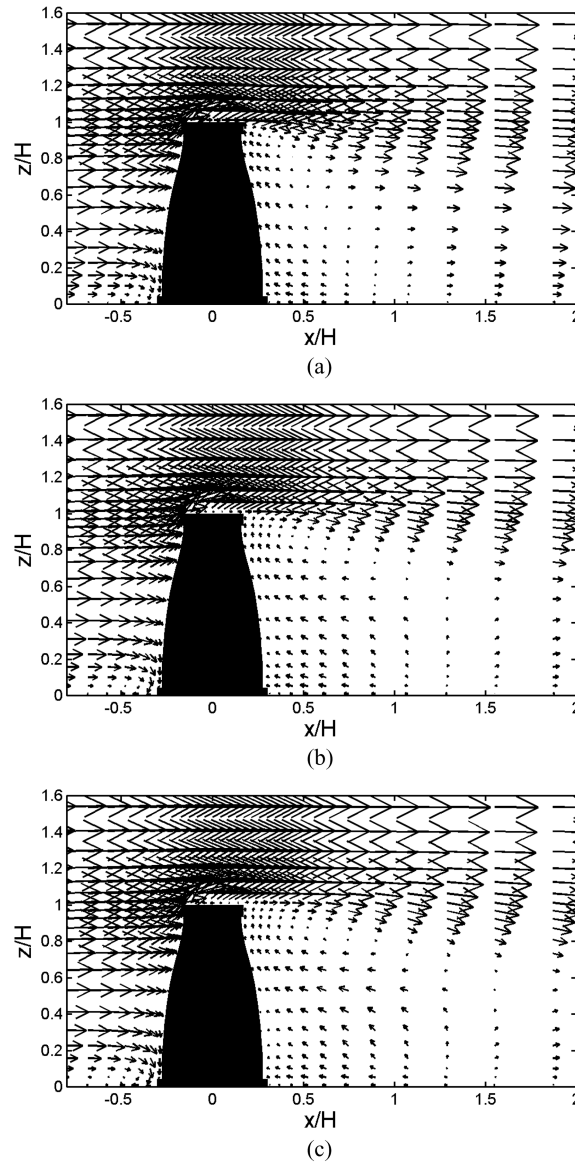
Fig. 6 Wind vector fields at $y/H = 0$ in the experiments with $U_r =$ (a) 1 m s^{-1} (experiment S1), (b) 3 m s^{-1} (experiment S2), and (c) 7 m s^{-1} (experiment S3). The maximum wind vector lengths in (a), (b), and (c) are 1.49, 4.47, and 10.42 m s^{-1}, respectively

the results from the experiments with different ambient wind speeds, an increase in ambient turbulence intensity results in a decrease in the size of the recirculation zone. This is consistent with the result of Kim, *et al.* (2001).

Fig. 7(a) shows the opposing effects of ambient wind speed and turbulence intensity on the predicted size of the recirculation zone behind Cheomseongdae. To take account of the effects of these two factors together, we define the effective Reynolds number Re for a given space (S) as
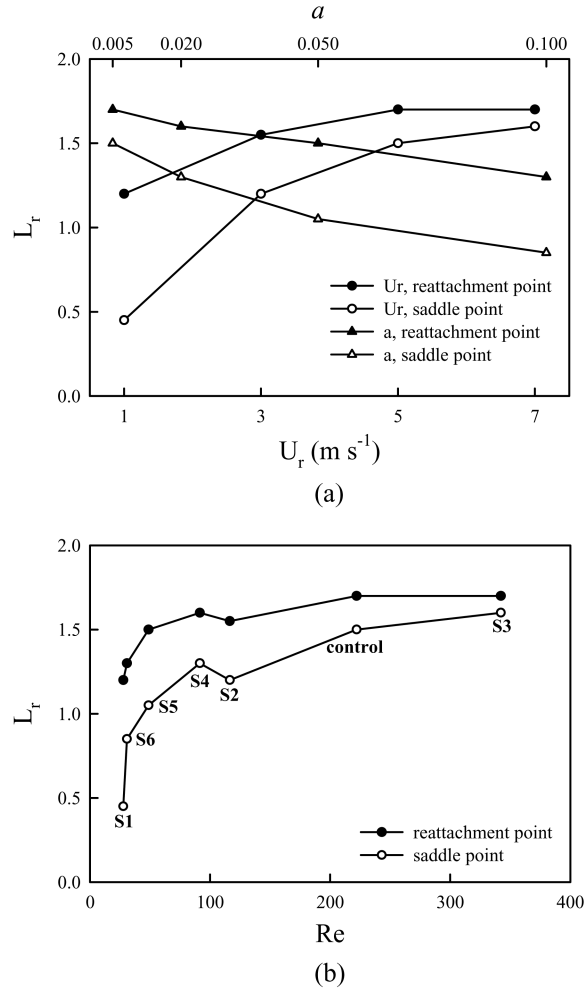
Fig. 7 Distances to the flow reattachment point on the ground surface and saddle point from the center of Cheomseongdae as a function of (a) ambient wind speed and turbulence intensity and (b) effective Reynolds number

$$\text{Re} = \frac{\overline{V}H}{\overline{v}_t} \qquad (4)$$

where $\overline{V}$ is the average mean wind speed given by

$$\overline{V} = \frac{1}{S}\int_S V ds \qquad (5)$$

and $\overline{v}_t$ is the average turbulent diffusivity

$$\overline{v}_t = \frac{1}{S}\int_S v_t ds \qquad (6)$$

H in Eq. (4) is the height of Cheomseongdae. Noticing that the flow state upwind of

Cheomseongdae is important for flow downwind, the spatial average is taken for a region defined by $-1 \leq x/H \leq 0$, $-0.5 \leq y/H \leq 0.5$, and $0 \leq z/H \leq 1$. Fig. 7(b) shows the distance to the saddle point and the flow reattachment point on the ground surface as a function of the effective Reynolds number. As Re increases, the distance to the saddle point (also the flow reattachment point) increases except for the case of experiment S2. This implies that inertial force plays a role in increasing the distance, while eddy force decreases the distance. Also, it is implied that flow with relatively strong inertial force can produce a recirculation zone above the roof by enhancing flow
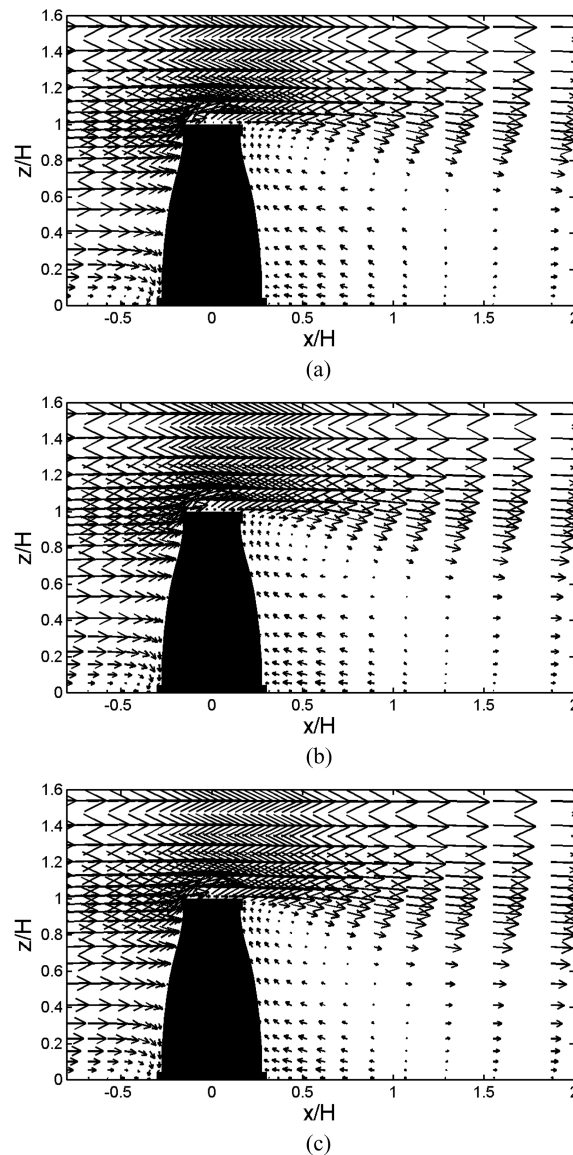

(a)

(b)

(c)

Fig. 8 Wind vector fields at $y/H = 0$ in the experiments with $a =$ (a) 0.02 (experiment S4), (b) 0.05 (experiment S5), and (c) 0.10 (experiment S6). The maximum wind vector lengths in (a), (b), and (c) are 7.44, 7.43, and 7.42 m s^{-1}, respectively
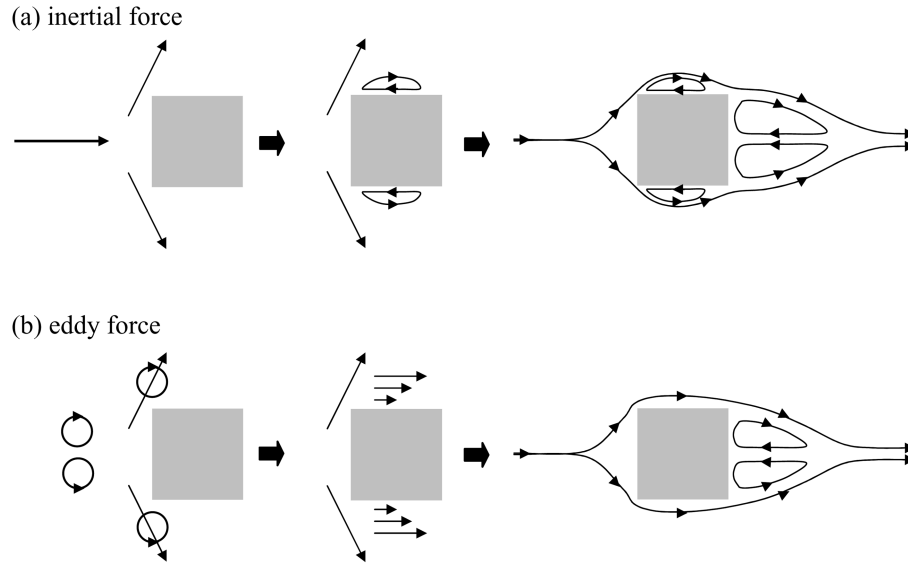
(a) inertial force

(b) eddy force

Fig. 9 Sketch for explaining the roles of (a) inertial and (b) eddy forces in forming cavity boundary around an obstacle

separation there (Figs. 4(b), 6, and 8).

Based on the above results, we present a schematic illustration that explains the roles of inertial and eddy forces in forming cavity boundary around an obstacle (Fig. 9). When flow impinges on an obstacle, flow separation occurs and thus a separation boundary is formed. As inertial force increases, flow separation is promoted further. Consequently, cavity flow zones around the obstacle expand and flow reattachment occurs farther downwind. On the other hand, as eddy force increases, flow separation zones contract by mixing momentum there. This causes cavity flow zones to contract and flow reattachment occurs less far downwind.

To compare the overall characteristics of scalar dispersion in the experiments with different inflow boundary conditions, scalar concentration in each of experiments S3, S2, S6, and S1 is plotted against that in the control experiment (Fig. 10). Here, scalar concentration values exceeding 1 ppb for all grid points are selected and plotted. Also, plotted is the scalar concentration difference field at $z/H = 0.49$ between each of experiments S3, S2, S6, and S1 and the control experiment (Fig. 11).

When the effective Reynolds number is larger than that in the control experiment (as in experiment S3), scalar advection becomes stronger and scalar concentration in most regions is lower than that in the control experiment (Fig. 10(a)). The maximum scalar concentration is also lower. In the region from near the scalar source point to the upwind face of Cheomseongdae, scalar concentration is higher in experiment S3 than in the control experiment (Fig. 11(a)). Scalar advection in experiment S2 is weaker than that in the control experiment. Hence, scalar concentration in most regions and its maximum are larger in experiment S2 than in the control experiment (Fig. 10(b)). The scalar concentration in the region from near the scalar source point to the upwind face of Cheomseongdae is lower in experiment S2 than in the control experiment (Fig. 11(b)). This lower scalar concentration region closely corresponds to the higher scalar concentration region in experiment S3 (Figs. 11(a) and 11(b)). When the effective Reynolds number is smallest (experiment S1), the scalar concentration is higher in most regions than that in the control experiment and its
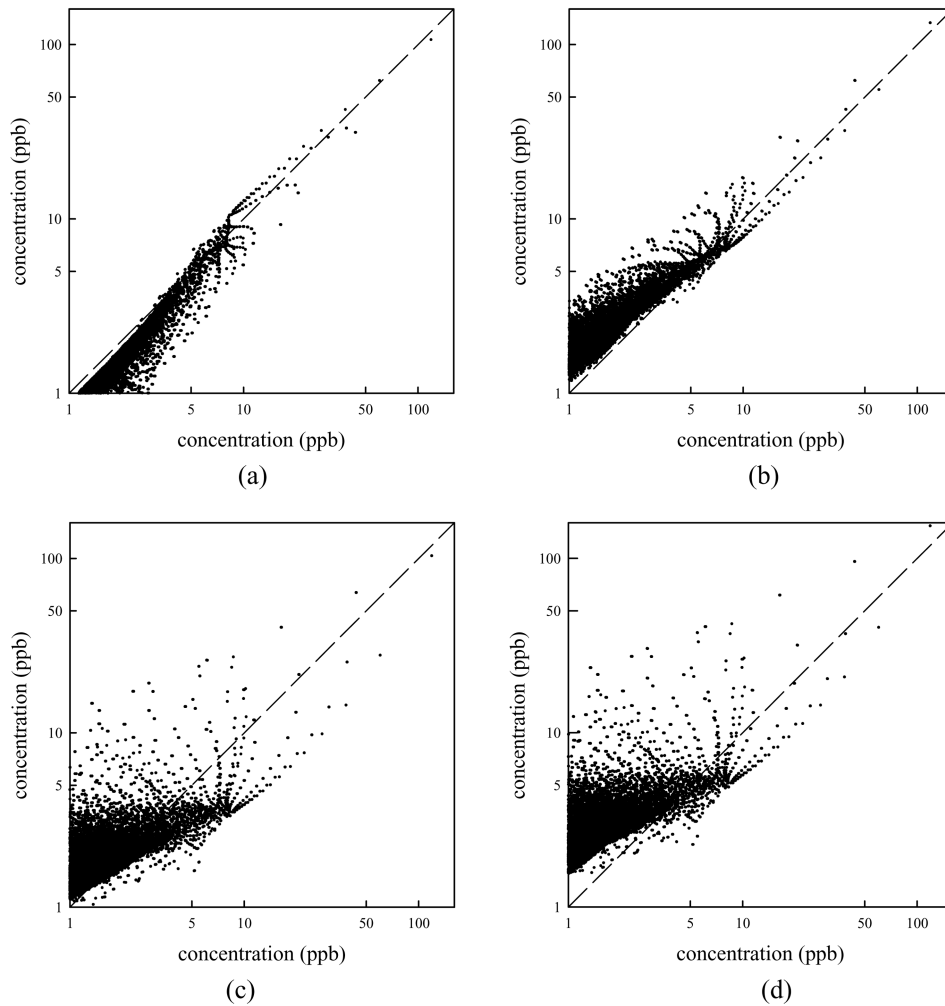
Fig. 10 Scalar concentration in the control experiment (horizontal axis) versus that in experiment (a) S3, (b) S2, (c) S6, and (d) S1 (vertical axis)

increase is largest among the four experiments (Fig. 10(d)). The maximum scalar concentration in experiment S1 is higher than that in the control experiment. As in experiment S2, the scalar concentration in the region from near the scalar source point to the upwind face of Cheomseongdae is lower than that in the control experiment (Fig. 11(d)). Figs. 10(a), 10(b), and 10(d) show that a decrease in ambient wind speed results in an increase in scalar concentration in most regions. Notice that experiments S3, S2, and S1 have the same inflow turbulence intensity but have different inflow wind speeds.

In experiment S6 that has the same inflow wind speed as in the control experiment but has stronger inflow turbulence intensity, relatively high concentration (that is, larger than 4 ppb) tends to decrease in comparison with high concentration in the control experiment (Fig. 10(c)). On the other hand, low concentration (that is, less than 4 ppb) tends to increase in comparison with low concentration in the control experiment (Fig. 10(c)). This is because advective effects are similar in
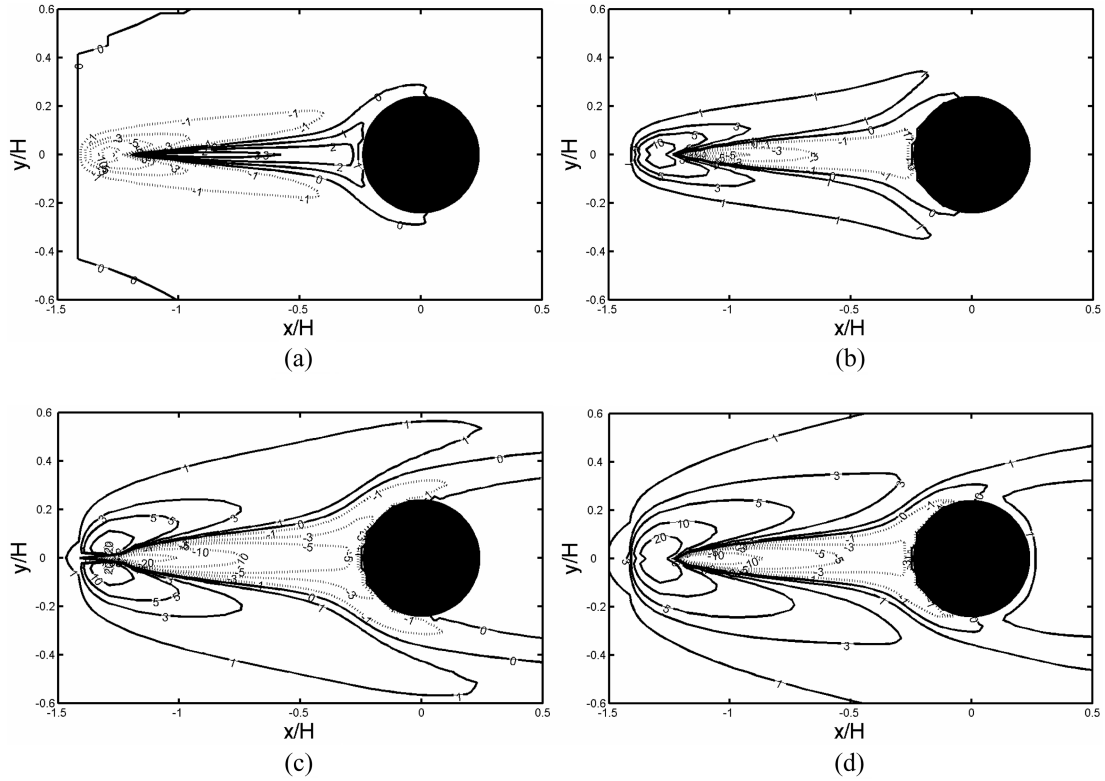
Fig. 11 Concentration difference fields (in ppb) at $z/H = 0.49$ between experiment (a) S3, (b) S2, (c) S6, and (d) S1 and the control experiment

experiment S6 and the control simulation, but in experiment S6 turbulent diffusivity is larger due to stronger turbulent kinetic energy (Kim and Baik 2003), resulting in a decrease (an increase) in scalar concentration for high (low) concentration. The maximum scalar concentration in experiment S6 is lower than that in the control experiment. Thus, it is suggested that such a scalar distribution in Fig. 10(c) results from a turbulent diffusion process that acts to distribute scalars more evenly. Figs. 10 and 11 indicate that an increase in ambient wind speed lowers scalar concentration and that an increase in ambient turbulence intensity lowers maximum scalar concentration and acts to distribute scalars evenly.

5. Conclusions

This study numerically examined flow and scalar dispersion around Cheomseongdae using a three-dimensional computational fluid dynamics (CFD) model. Cheomseongdae was chosen as a model obstacle because of its unique shape. A saddle point at the middle height behind Cheomseongdae was detected. It was shown that the size of the recirculation zone formed behind Cheomseongdae increases with increasing ambient wind speed and decreases with increasing ambient turbulence intensity. The relative roles of inertial and eddy forces in producing cavity flow zones around an obstacle were conceptually presented. It was demonstrated that an increase in

ambient wind speed reduces scalar concentration and that an increase in ambient turbulence intensity reduces maximum scalar concentration and distributes scalars more evenly. The results from this study are expected to provide additional insights into flow and scalar dispersion around obstacles.

Acknowledgements

References

Becker, S., Lienhart, H., and Durst, F. (2002), "Flow around three-dimensional obstacles in boundary layers", *J. Wind Eng. Ind. Aerodyn.*, **90**, 265-279.

Brown, A.L. and Dabberdt, W.F. (2003), "Modeling ventilation and dispersion for covered roadway", *J. Wind Eng. Ind. Aerodyn.*, **91**, 593-608.

Brown, M.J., Lawson Jr. R.E., DeCroix, D.S., and Lee, R.L. (2000), "Mean flow and turbulence measurements around a 2-D array of buildings in a wind tunnel", *11th Joint Conference on the Applications of Air Pollution Meteorology with the A&WMA*, Long Beach, January.

Castro, I.P. and Apsley, D.D. (1997), "Flow and dispersion over topography: A comparison between numerical and laboratory data for two-dimensional flows", *Atmos. Environ.*, **31**, 839-850.

Chan, A.T., So, E.S.P., and Samad, S.C. (2001), "Strategic guidelines for street canyon geometry to achieve sustainable street air quality", *Atmos. Environ.*, **35**, 5681-5691.

Higson, H.L., Griffiths, R.F., Jones, C.D., and Hall, D.J. (1994), "Concentration measurements around an isolated building: A comparison between wind tunnel and field data", *Atmos. Environ.*, **28**, 1827-1836.

Hussein, H.J. and Martinuzzi, R.J. (1996), "Energy balance for turbulent flow around a surface mounted cube placed in a channel", *Phys. Fluids*, **8**, 764-780.

Jiang, Y., Alexander, D., Jenkins, H., Arthur, R., and Chen, Q. (2003), "Natural ventilation in buildings: Measurement in a wind tunnel and numerical simulation with large-eddy simulation", *J. Wind Eng. Ind. Aerodyn.*, **91**, 331-353.

Jones, C.D. and Griffiths, R.F. (1984), "Full-scale experiments on dispersion around an isolated building using an ionized air tracer technique with very short averaging time", *Atmos. Environ.*, **18**, 903-916.

Kim, J.-J., Baik, J.-J., and Chun, H.-Y. (2001), "Two-dimensional numerical modeling of flow and dispersion in the presence of hill and buildings", *J. Wind Eng. Ind. Aerodyn.*, **89**, 947-966.

Kim, J.-J. and Baik, J.-J. (2003) "Effects of inflow turbulence intensity on flow and pollutant dispersion in an urban street canyon", *J. Wind Eng. Ind. Aerodyn.*, **91**, 309-329.

Kim, J.-J. and Baik, J.-J. (2004), "A numerical study of the effects of ambient wind direction on flow and dispersion in urban street canyons using the RNG $k - \varepsilon$ turbulence model", *Atmos. Environ.*, **38**, 3039-3048.

Lübcke, H., Schmidt, S., Rung, T., and Thiele, F. (2001), "Comparison of LES and RANS in bluff-body flows", *J. Wind Eng. Ind. Aerodyn.*, **89**, 1471-1485.

Meroney, R.N., Leitl, B.M., Rafailidis, S., and Schatzmann, M. (1999), "Wind-tunnel and numerical modeling of flow and dispersion about several building shapes", *J. Wind Eng. Ind. Aerodyn.*, **81**, 333-345.

Nigim, H.H. (1996), "Recovery of equilibrium turbulent boundary layers downstream of obstacles", *Phys. Fluids*, **8**, 548-554.

Patankar, S.V. (1980), *Numerical Heat Transfer and Fluid Flow*, McGraw-Hill, New York.

Sada, K. and Sato, A. (2002), "Numerical calculation of flow and stack-gas concentration fluctuation around a cubical building", *Atmos. Environ.*, **36**, 5527-5534.

Smith, W.S., Reisner, J.M., and Kao, C.-Y.J. (2001), "Simulations of flow around a cubical building: Comparison with towing-tank data and assessment of radiatively induced thermal effects", *Atmos. Environ.*, **35**, 3811-3821.

Tutar, M. and Oguz, G. (2002), "Large eddy simulation of wind flow around parallel buildings with varying configurations", *Fluid Dyn. Res.*, **31**, 289-315.
Yakhot, V. and Orszag, S.A. (1986), "Renormalization group analysis of turbulence", *J. Sci. Comp.*, **1**, 3-51.
Yakhot, V., Orszag, S.A., Thangam, S., Gatski, T.B., and Speziale, C.G. (1992), "Development of turbulence models for shear flows by a double expansion technique", *Phys. Fluids*, **A4**, 1510-1520.

CC